Developmental Cell
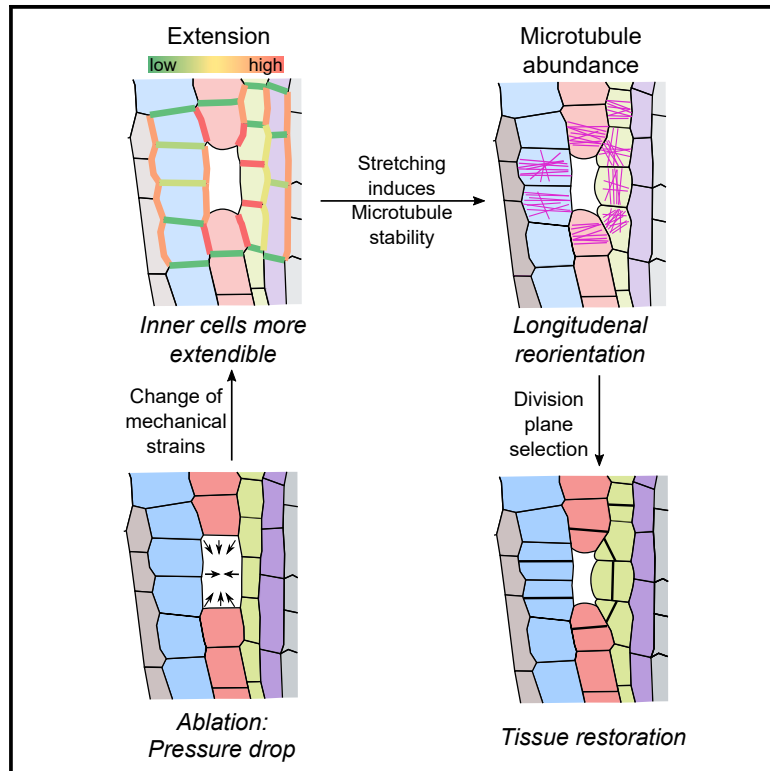
Mechanical forces in plant tissue matrix orient cell divisions via microtubule stabilization

Graphical abstract

Highlights

- Mechanical forces determine cell division planes in root cells

- High cellular tension in plant cells, e.g., via stretching, stabilizes microtubules

- Inner root cell matrix is more extendible and stretchable than outer cells

- Higher microtubule abundance in stretched cell parts leads to division reorientation

Authors

Lukas Hoermayer,
Juan Carlos Montesinos,
Nicola Trozzi, ..., Yasin Dagdas,
Mateusz Majda, Jiří Friml

Correspondence

jiri.friml@ist.ac.at

In brief

Hoermayer et al. show how mechanical forces drive immobile plant cells to flexibly arrange division plane orientations and tissue expansion directions. They demonstrate that increased mechanical strain, e.g., through stretching and cellular deformation, stabilizes microtubule bundles, resulting in changed orientations ultimately altering division plane orientations.

CelPress

Article

Mechanical forces in plant tissue matrix orient cell divisions via microtubule stabilization

Lukas Hoermayer,[1,2,3] Juan Carlos Montesinos,[1,4] Nicola Trozzi,[2] Leonhard Spona,[1] Saiko Yoshida,[1,5] Petra Marhava,[1,6] Silvia Caballero-Mancebo,[1] Eva Benková,[1] Carl-Philip Heisenberg,[1] Yasin Dagdas,[3] Mateusz Majda,[2] and Jiří Friml[1,7,*]

[1]Institute of Science and Technology Austria (ISTA), 3400 Klosterneuburg, Austria
[2]Department of Plant Molecular Biology (DMBV), University of Lausanne, 1015 Lausanne, Switzerland
[3]Gregor Mendel Institute (GMI), Austrian Academy of Sciences, Vienna BioCenter, Vienna, Austria
[4]Instituto Universitario de Biotecnología y Biomedicina (BIOTECMED), Departamento de Bioquímica y Biología Molecular, Universitat de València, 46100 Burjassot, Spain
[5]Max Planck Institute for Plant Breeding Research, 50829 Carl-von-Linné-Weg 10, Cologne, Germany
[6]Umeå Plant Science Centre (UPSC), Department of Forest Genetics and Plant Physiology, University of Agricultural Sciences (SLU), 90183 Umeå, Sweden
[7]Lead contact
*Correspondence: jiri.friml@ist.ac.at
https://doi.org/10.1016/j.devcel.2024.03.009

SUMMARY

Plant morphogenesis relies exclusively on oriented cell expansion and division. Nonetheless, the mechanism(s) determining division plane orientation remain elusive. Here, we studied tissue healing after laser-assisted wounding in roots of *Arabidopsis thaliana* and uncovered how mechanical forces stabilize and reorient the microtubule cytoskeleton for the orientation of cell division. We identified that root tissue functions as an interconnected cell matrix, with a radial gradient of tissue extendibility causing predictable tissue deformation after wounding. This deformation causes instant redirection of expansion in the surrounding cells and reorientation of microtubule arrays, ultimately predicting cell division orientation. Microtubules are destabilized under low tension, whereas stretching of cells, either through wounding or external aspiration, immediately induces their polymerization. The higher microtubule abundance in the stretched cell parts leads to the reorientation of microtubule arrays and, ultimately, informs cell division planes. This provides a long-sought mechanism for flexible re-arrangement of cell divisions by mechanical forces for tissue reconstruction and plant architecture.

INTRODUCTION

Cells in plants are fixed in their relative position within a tissue; they are surrounded by a cell wall matrix that prevents cell migration, limits their expansion, and glues them together. Owing to this immobility, oriented cell division and expansion are important determinants of morphogenesis. Division plane orientation defines how two daughter cells will be spatially separated; hence, it is crucial for cell-type acquisition and tissue development.[1–3]

A crucial developmental process relying on precisely executed and directed cell divisions is wound healing, where damaged patches of cells are replaced by proliferating cells.[4–6] Recently, we introduced an experimental setup of cell ablation in the root meristem that allows the investigation of tissue restoration on a cellular level, *in situ,* and in real time.[7,8] Our studies identified the phenomenon of restorative divisions, where cells switch division planes to invade and replace dead cells through subsequent cell expansion and cell fate acquisition. These restorative divisions occur predominantly at the inner adjacent side of the wound and show similarities to the regeneration of whole-root excisions.[7–11] However, the underlying mechanism behind pre-cisely executed cell divisions and their exclusive occurrence in inner adjacent cells remains elusive.

How cell division planes are placed in root tissues is crucial for regulating tissue architecture[1,2,12,13] and the outgrowth of new organs like the lateral root.[14–16] Hence, division plane selection is highly regulated and multiple influencing factors have been described: geometry, developmental cues, local and tissue-derived stress.[3] The default choice for the cell division plane is determined by the cell geometry: a plant cell divides through one of its shortest axes, minimizing the new cell wall area.[17,18] However, this rule does not explain the orientation of divisions in most plant cells. Developmental cues may override the division plane selection through gene expression or localization of polarity-defining proteins, e.g., during formative divisions in stem cells and throughout embryo development.[12,19–24] However, such developmental cues only mildly affect the division plane switch after cell ablation,[7] suggesting greater importance of alternative factors driving division plane selection in the root.

Plant cells undergo a variety of local and tissue-derived stresses that may alter or influence division planes more directly. Wound-adjacent cells respond to ablation through expression of stress-related genes like ethylene response factor 115

(ERF115)[7,25,26] and expansion toward the wound.[8] Plant cells are exposed to a high turgor pressure that generates mechanical stress on surrounding walls, which can be minimized by expansion.[27–29] In cells with homogeneous mechanical properties growing isotropically, the shortest division path follows the direction of maximal tensile stress patterns.[30,31] However, when the growth is anisotropic in tissues like the shoot apical meristem, division planes and microtubules (MTs) align with tensile stress derived from the tissue growth,[32,33] and similar behavior of the MT cytoskeleton in response to tensile stress has been shown in stem apices, hypocotyls, sepals, and leaves.[34–39]

MTs are cytoskeletal filaments that are involved in guiding the deposition of cellulose microfibrils[40] and mark the future position of the division plane in proliferating tissues.[41] The cellulose microfibrils in the cell wall act as springs, restricting growth leading to polarized shapes and anisotropic growth, linking MT orientation with cell expansion direction. *In vitro* MT growth assays have shown that their stability is altered by stretching,[42–44] suggesting that they may act as tensile stress sensors.[45] However, a possible mechanism linking tissue mechanical properties, cell expansion, and cell division plane switches during tissue development remains elusive.

In this study, we used cell ablation coupled with high-resolution and real-time imaging to study division plane switches during restorative cell divisions. We show that the whole tissue deforms, which is transmitted into the reorientation of division planes in individual cells around the wound. This occurs via the re-arrangement of MT arrays. Accordingly, MT stability is dependent on cell expansion, and cell stretching by wounding or through external aspiration promotes MT bundle formation. Our results identify a mechanism by which cell expansion, via stretching forces, reorients MTs and orients cell division planes for tissue architecture.

RESULTS

Direction of cell expansion correlates with division plane orientation

Tissue regeneration in the root meristem involves induction of divisions and reorientation of division planes around the wound.[7] To identify potential local and cell-cell communication mechanisms in response to wounds, we investigated the involvement of chemical signaling and found an accumulation of both cytosolic calcium (Ca^{2+}) and reactive oxygen species (ROS; such as hydrogen peroxide H_2O_2). We observed the induction of Ca^{2+} waves starting instantly (within 0.2 s) from the ablated cells, transmitted through the adjacent cells, and reaching the whole-root tip within 20 s (Figure S1A). Additionally, we observed an accumulation of H_2O_2 around the wound reaching a 1.22 ± 0.12-fold increase within 18 min (Figure S1B). However, the Ca^{2+} waves observed here did not correspond to the spatially restricted occurrence of restorative divisions. We also have previously shown that exogenous treatment of roots with H_2O_2 did neither induce wound responses like ERF115 nor trigger division plane changes.[8] Additionally, when we applied an extract of wounded root tips, we did not observe upregulation of *ERF115::GFP* nor did the root extract induce any division plane changes (Figure S1C). These experiments did not identify any causative chemical wound signal-inducing restorative divisions.

Hence, we focused on mechanical forces that may be involved and investigated the interdependence of cell expansion and restorative divisions by high-resolution three-dimensional (3D) imaging. Notably, we observed division plane changes from anticlinal to periclinal in endodermal cells that were not in direct contact with the ablated cortical cells (Figure 1A, white arrows). These pairs of cells increased in cell width compared with other endodermal (green) cells in the same roots. Top view sections showed that the width increased throughout the whole length compared with neighboring cells, marking an increase in cell volume (Figure 1B, white arrows). Cells directly in contact with ablated cells increased similarly in width and volume (Figures 1A and 1C, red arrows). To further investigate this phenomenon, we used long-term time-lapse imaging of wounded roots at the vertical stage microscope. This showed that such non-adjacent cells undergo a constant cell expansion toward the wound (expansion rate was 1.44 times in 8.2 h before division, Figures 1D and 1E). However, this expansion was significantly slower than the cell expansion observed for adjacent cells (1.47 times in 5 h) (Figures 1D, 1E, and S1D). As control, we analyzed the expansion of a neighboring cell that was more distant to the cell ablation than the non-adjacent cell. This neighboring cell expanded significantly less than the non-adjacent and adjacent cell (1.13 times in 9.8 h), and no alteration of the pre-established anticlinal cell division plane was observed (Figures 1D, 1E, and S1D; Video S1). This suggests that it is not merely a direct connection to the wound that induces division plane changes but expansion toward the wound.

Here, we identified that cellular deformation drives the orientation of division planes, either during invasion of the wound area or by indirect deformation from the adjacent tissue. Our results show how even cells non-adjacent to the wound increase in cell width, followed by a change of division plane orientation in these cells. Mechanical perturbations affecting division planes in distant cells have been shown in the shoot apical meristem[32,33] in accordance with our observations here, after ablations in the root meristem.

Wounding induces immediate outward tissue and cell deformation

The dependence of division plane changes on directional expansion or stretching motivated us to investigate the changes in mechanical properties of root tissues after wounding. We have previously shown that cell ablation causes an instantaneous pressure loss at the wound site.[8] By time-lapse imaging, we found that the surrounding cells rapidly deformed toward the wounds within 20 min (Figure 2A). Cells that were not in contact with the wound also deformed toward the wound quickly (Figure 2B; Video S2), suggesting that pressure changes and the resulting tension release immediately cause tissue deformation. However, the displacement of cells was not homogenous. In comparison with the slight deformation of outer cells, the inner wound-adjacent cells deformed significantly more toward the wound, (Figures 2A–2C), which suggests different mechanical properties in cells across different tissues[46] and/or gradients in compression-tension within the root.[47] To further dissect this phenomenon, we ablated two cell types simultaneously, the outer epidermis and inner endodermis, with intact cortical cells in between. The first respective inner adjacent cells intruded into the space of both ablated cell types (Figures S2A–S2D).
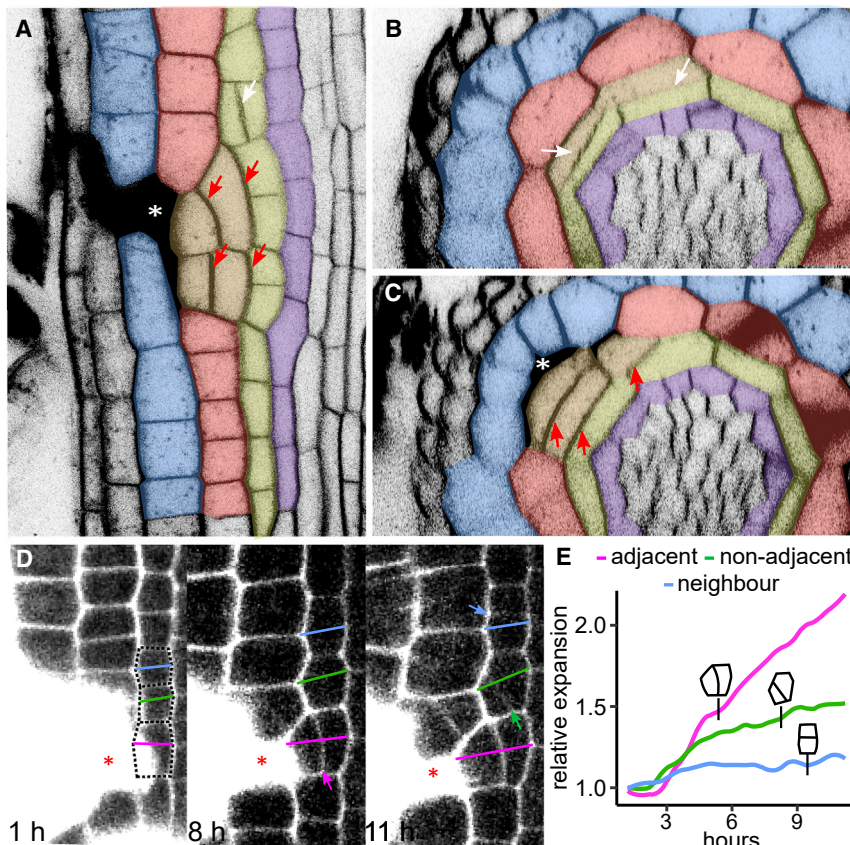
Figure 1. Division orientation defined by directional cell expansion

(A–C) Non-wound-adjacent cells trigger division plane switch 24 h after cortical and epidermal ablation. (A) Front view with periclinal divisions of wound-adjacent (red arrows) and non-adjacent (white arrows) endodermis. (B) Top view of non-adjacent endodermal cells (white arrows). (C) Top view showing the ablation after periclinal divisions in the endodermis (red arrows). Plasma membranes of root cells were stained with FM4-64. Cell types were re-colorized as epidermis (blue), cortex (red), endodermis (green), and pericycle (purple).

(D and E) Non-adjacent periclinal divisions are preceded by cell expansion. (D) Time series of cell expansion close to ablation in PI-stained root tip. Maximum cell width is drawn as a line: magenta for adjacent cell, green for non-adjacent cell, and blue for distant neighbor. Divisions are marked by arrows. (E) Quantification of cell width from (D) and time point of division. Graph is a representative example (full quantification see Figure S1D). Asterisks mark ablated cells.

See also Video S1.

Division plane is determined by a transient reorientation of MT arrays

Our results suggest that the induction of restorative divisions and the inherent division plane switch depend on cell expansion and a cell's underlying physical deformations. However, the cellular and molecular machinery behind the division plane switch remains elusive. To address that, we first investigated the possibility of switching division plane orientation throughout the cell cycle, mainly the M phase, where cytokinesis occurs, and the directly preceding phase, G2.

We monitored the different cell division stages using the MTs' marker line *35S::MAP4-GFP*[49] and observed that adjacent cells already in mitosis were not able to switch their division plane (Figures S3A and S3B). However, the spindles were highly tilted compared with control cells without ablations (Figure S3A; Video S4. During cell division, the MT-rich pre-prophase band (PPB) marks the future cell division plane.[41] Wound-adjacent cells with already established PPB at the moment of ablation divided without reorienting the cell division plane (Figures S3C and S3D). However, using the G2-phase marker *CYCB1;1::GFP*,[50] we observed wound-adjacent cells in the G2 phase with high CYCB1;1 expression that still performed a division plane switch (Figures S3E and S3F). These findings suggest that the orientation of division planes can still be switched late in the cell cycle, during the transition to the G2 phase. Although the role of the PPB in fixing the orientation of division is disputed, and cells without PPB do not show defects in normal division orientation[51] or division plane reorientation,[8] the appearance of the PPB can be used to mark a time point when the cortical division zone is already established and the orientation of the cell division plane after ablation cannot be redefined anymore.

This result confirms that the inner cells deform more in response to cell ablation, taking priority in the response to wounding.

To further investigate why inner cells deform and expand more toward wounds than outer cells, we ablated a horizontal section of cells, mimicking a macroscopic root tip excision (Figure 2D). Intact cells around the ablation immediately deformed toward the wounded area (Figure 2E; Video S3). The resulting cell displacement was stronger in cells of the stele, with a decreasing displacement of the outer cell types (Figure 2F). Notably, the displacement was transmitted also to cells further away from the ablation, reaching furthest in stele cells (Figures S2E–S2H). When we quantified the deformation coefficients after the subsequent ablation of two cells from the outer cell files (epidermis and cortex), we also found that the inner tissues displaced significantly more toward the wound while outer cells stayed in place (Figures S2I–S2K; Video S2), suggesting that the inner tissues are exposed to higher compressional forces that can be released upon cell ablation. Such a mechanical heterogeneity in cells of cylindrical plant organs has been recently implied in stem development,[48] where specifically inner cells are under compressive stress. This implies that in the root, inner tissues act like an extendable matrix with an increased capacity to deform compared with outer tissues.

Here, we identified a tissue extendibility gradient within the root of more deforming inner cells compared with more rigid outer cells. This differential extensibility within the root is consistent with the preferential response of inner tissues in mediation of the restorative cell divisions that occur in response to wounding.
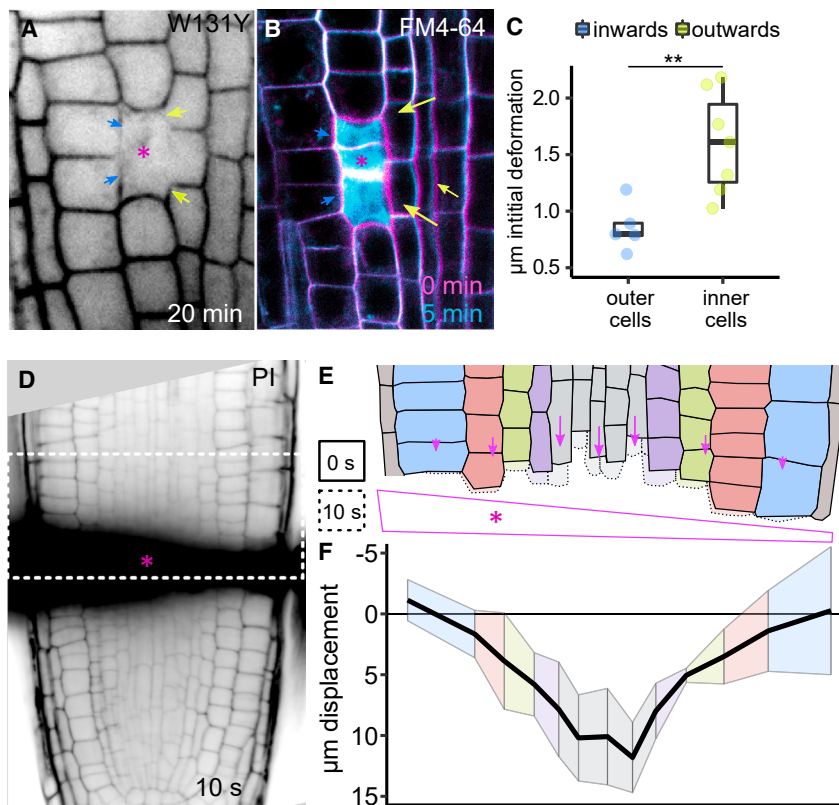
Figure 2. Instant, wound-induced deformations of root cells

(A–C) Root cell deformations induced after wounding. (A) *W131Y* plasma membrane marker 20 min after ablation. (B) Time series overlay of cortical cell ablation directly before death (magenta) and 5 min after death (cyan). Plasma membranes were stained with FM4-64. Arrows indicate displacement of membranes from inner (yellow) and outer (blue) cells. (C) Quantification of displacement in µm within first 20 min after ablation in outer (blue) wound-adjacent cells inward, and in inner (yellow) wound-adjacent cells outward (n = 7–8 cells each). Asterisks mark ablated cells.

(D–F) Extendibility of cells within the root meristem. (D) PI-stained root tip 10 s after ablation of a horizontal row of cells (black area around asterisk). White dashed rectangle indicates a redrawn image in (E). (E) Redrawn section from (D) above horizontal ablation (marked as a purple area with an asterisk) before ablation (full lines) and 10 s after ablation (dashed lines). Arrows indicate displacement. (F) Quantification of displacement toward the wound in µm from (E). Black line indicates the mean and colored ribbon indicates 95% CI from n = 3 roots. Cell types were colorized as epidermis (blue), cortex (red), endodermis (green), pericycle (purple), and stele (gray).

See also Figure S2 and Videos S2 and S3.

Hence, we investigated the transition of cortical MT arrays to organized PPB rings. In the root meristem, cortical MTs visualized by the 35S::MAP4-GFP marker line are oriented in weakly defined transverse arrays (Figures 3Ai and 3Aii). Wound-adjacent cells underwent a re-arrangement of cortical MT orientation. First, a new array of longitudinal cortical MTs appeared (Figure 3Aiii); second, a depletion of transversal MT arrays, followed by the PPB formation in a new orientation (periclinal), was observed (Figure 3Aiv). Notably, time-lapse imaging showed that longitudinal arrays appeared when transversal arrays were still present and co-existed for an additional 2.0 h before the PPB formed (Figure 3B). We observed individual MT arrays during this co-existence phase and found multiple orientations of transversal, longitudinal, and oblique bundles within the same cell (Figure 3C). Due to the small size of meristematic root cells and their stacked arrangement, reliable quantification of cortical orientations was technically not possible; hence, we measured the fluorescence signal intensity on the membranes instead. The ratio of longitudinal versus transversal MT intensity was significantly higher in wound-adjacent cells (0.88 ± 0.122) compared with control cells (0.43 ± 0.147) (Figure 3D, left). In a control experiment, we observed a similar co-existence of different MT orientations in the MTs' marker line *UBQ10::Venus-TUA6* (Figures S3G and S3H).

To investigate the origin of these multiple MT array orientations, we observed wound-adjacent cells after MT depolymerization events. After the first division, where mitosis causes total depletion of MTs in the cell, the wound-adjacent daughter cells still displayed multiple MT orientations (Figures 3D middle and S3I). When we exogenously depolymerized MT cortical arrays using the depolymerization drug oryzalin,[52] and let the MT arrays re-polymerize after washout, we also observed multiple cortical MT orientations in wound-adjacent cells (Figures 3D right, and S3J; Video S5). Notably, oryzalin-treated roots displayed normal wound-responsive expansion and MTs oriented independently of actin polymerization status (Figures S3K and S3L).

These findings identified that wound-adjacent cells switch MT orientation transiently from transversal to a mixed population of transversal and longitudinal arrays before a complete switch to longitudinal orientation, which corresponds with a subsequent division plane switch. These multiple MT arrangements occurred independently of depolymerization events.

MT abundance correlates with cell expansion

Wound-induced release of the turgor pressure leads to deformation and expansion of surrounding cells toward the wound, affecting the stress patterns and the cells' shapes. The observed multiple orientations of cortical MT arrays in wound-adjacent cells could be a result of the change in the distribution of native stress patterns within the tissue. The longitudinal MT arrays may arise as a response to mechanical stress from the wound and the transversal arrays may be caused by the stress from the growing organ. To investigate this, we inhibited organ growth of the root meristem by perturbing cell expansion and observed the MT array distribution in response.

Auxin inhibits cell expansion in the root elongation and transition zones (TZ).[53,54] We observed similar inhibition of cell elongation in the meristem zone (Figures S4A–S4C). This inhibited cell
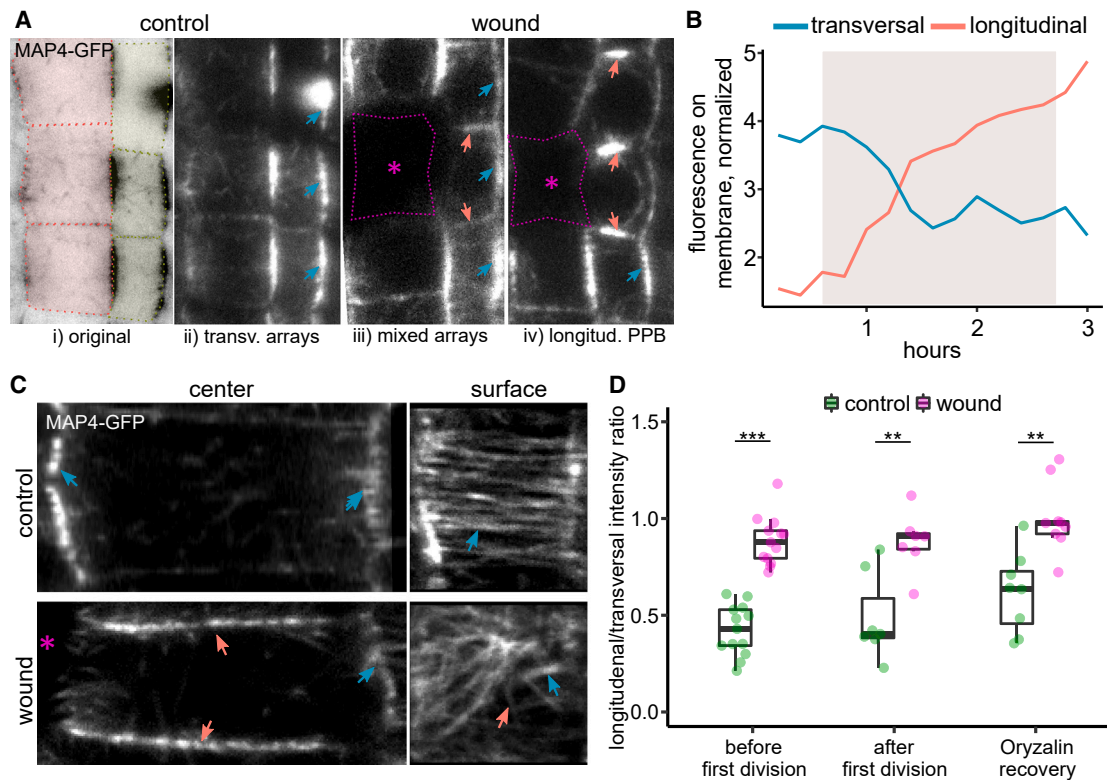
Figure 3. Wound-induced transient reorientation of MT arrays during restorative cell divisions

(A and B) Cortical MT array changes during restorative divisions. (A) From left to right: (i) transverse MT arrays as marked by 35S::MAP4-GFP in undisturbed cortex (red) and endodermis (green) cells; (ii) inverted picture of (i) without cell-type colorizing; (iii) wound-adjacent endodermal cell with longitudinal and transverse cortical MT arrangements; (iv) wound-adjacent endodermal cell with longitudinally localized PPB and neighboring cell with transverse arrays. Red and blue arrows indicate longitudinal and transversal arrays, respectively. Asterisks mark ablation. (B) Time-series quantification of 35S::MAP4-GFP fluorescence at transversal/lateral (blue line) and longitudinal/apical (red line) membranes over time from one representative wound-adjacent cell. Colored area indicates the co-existence of transversal and longitudinal arrays.

(C and D) Multiple orientations of cortically localized MT arrays. (C) MT arrays as marked by 35S::MAP4-GFP in control cortical cell (upper panels) and wound-adjacent cortical cell (lower panels). Left panels are from the center of the cell and the right panels are from the cell surface with visible cortical MT bundles. Blue and red arrows indicate transversal and longitudinal arrays or lateral and apical/basal membrane signals, respectively. Asterisks mark ablation. (D) Quantification of 35S::MAP4-GFP ratio between longitudinal (apical membrane) and transversal (lateral membrane) fluorescence; (from left to right) before division, after division, and during the recovery of the depolymerization induced by oryzalin 5 μM (12 h). Magenta represents wound-adjacent cells and green represents control cells from the same roots (n = 7–13 cells each).

See also Figure S3 and Video S5.

expansion was accompanied by a strong reduction of cortical MT arrays and an increase of cytosolic fluorescence signal in the 35S::MAP4-GFP marker line and, as control, also in the UBQ10::Venus-TUA6 marker line (Figures S4D and S4E). To manipulate cell expansion by independent means, we treated roots with the cellulose-biosynthesis-inhibitor isoxaben (IXB),[55] which also reduced cellular growth in the root tip (Figure S4F). Again, we observed a depletion of MT arrays during IXB treatment within 12 h (Figures S4G and S4H). Notably, cells in the TZ started to swell after prolonged growth inhibition, which was accompanied by an increased MT array abundance (Figure S4I). Our results suggest an interdependency of mechanical forces and stability of MT bundles. Hence, we investigated what happens to MT arrays during the rapid expansion of cells.

We first inhibited cell elongation by 12 h of auxin treatment and performed single-cell ablations to induce deformations. Any remaining transversal MT arrays completely disappeared

within 1 min after ablation (Figure S4J, left and middle panel) but notably re-polymerized within 15 min during the manifestation of the tissue deformation (Figure S4J, right panel). To further dissect this observation, we performed laser ablations with weaker pulses, where we induced a delayed cell death. The harmed cell collapsed 5–10 min after ablation and the wound-adjacent cells quickly deformed and stretched toward the wound (Figure 4A left and middle panel). Notably, MT bundles in these wound-adjacent cells reappeared at the very moment of deformation (Figure 4A middle panel). The de novo induced bundles moved from the cell interior toward the cortical membranes within 30 min (Figure 4A right panel, Video S6). Such induction of MT bundles after cell collapse was specific to directly adjacent cells (Figures 4B and 4C), suggesting that MT bundles are directly initialized and stabilized by a change of mechanical stress arising from the cell deformation toward the wound.
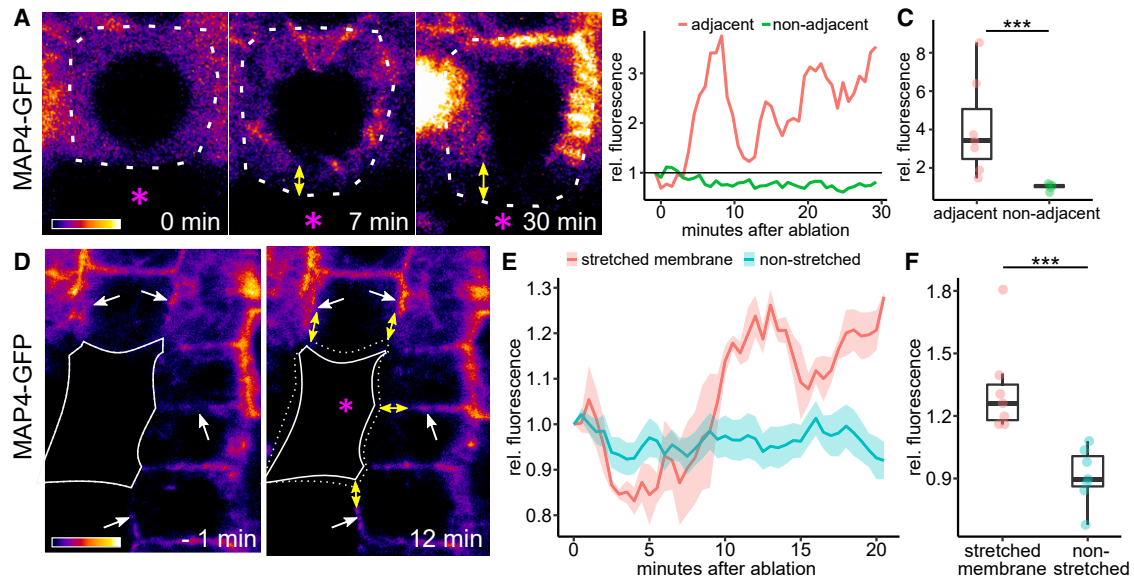
Figure 4. Induction of cell-localized MT polymerization by cell stretching

(A–C) MT polymerization is induced after the collapse of the ablated cell. (A) MT arrays in a cortical cell adjacent to UV-laser-harmed cell (asterisk). MT signal (*35S::MAP4-GFP*) before (left), during (middle), and after collapse of the ablated cell (right). Roots were pre-treated with 1 μM NAA for 12 h. Dotted line indicates the stretched cell. (B) Time series of cytosolic *35S::MAP4-GFP* signal (mean gray value relative to t_0) of a representative wound-adjacent cell during stretching (red line) caused by the collapse of an ablated cell and the closest neighbor non-adjacent to the collapsed cell (green line). (C) Quantification of the cytosolic *35S::MAP4-GFP* signal (mean gray value relative to t_0) directly after cell collapse in adjacent cells undergoing stretching (red dots) and in non-adjacent cells (green dots) (n = 7 cells each).

(D–F) MT stability is enhanced on stretched membranes. (D) *35S::MAP4-GFP*-marked MT arrays 1 min before collapse (left) and 12 min after the (right) collapse of the ablated cell. Yellow arrows mark stretched membranes and white arrows mark increased fluorescence at those membranes. White dotted line indicates the cell before collapse and the solid line indicates the cell after collapse. (E) Representative time series of membrane-localized *35S::MAP4-GFP* signal (mean gray value relative to t_0) from n = 3 cells adjacent to the ablation-induced cell collapse represented in (D). Stretched membrane signal (red line) and non-stretched membrane signal (blue line) have been taken from the same cells. Lighter background indicates standard error. (F) Quantification of the cortical *35S::MAP4-GFP* signal (mean gray value relative to t_0) 12 min after cell collapse in wound-adjacent cells undergoing stretching (red dots) and not undergoing stretching (blue dots) (n = 7 cells each).

See also Figure S4 and Video S6.

In a complementary experiment, we observed cortical MT abundance in cells around the wound before and after the cell collapse. Again, wound-adjacent cells were immediately deformed upon collapse of the ablated cell, and cell sides perpendicular to the wound area increased slightly in length (Figure 4D, yellow arrows). These stretched cell sides showed a significant increase of cortical MT signal in the *35S::MAP4-GFP* marker line (Figure 4D, white arrows, Figures 4E and 4F) 12 min after the collapse of the ablated cell. Non-stretched membranes of the same cells did not show any increase in cortical MT abundance (Figures 4E and 4F), suggesting a specific effect of collapse-induced stretching on cortical MT abundance.

Here, we identified a direct effect of mechanical stress, in the form of cell deformation after ablation, on MT abundance. Our results indicate that extended cells increase MT stability, causing an increased abundance of cortical MTs on stretched cell sides.

Mechanical forces during external stretching rapidly drive MT polymerization

To investigate more specifically whether MT polymerization is a response to mechanical forces of stretching, we adapted the micromanipulation-assisted micropipette aspiration system[56]

to plants and induced stretching of cells in living root tissue. To decrease the cell wall stiffness and turgor pressure, we employed a mix of macerozyme and mannitol solutions, which led to the MTs' depolymerization, preventing cortical arrays within roots (Figure 5A, left panel). Notably, aspiration of epidermal cells caused an increase of GFP signal within the aspirated part of the cell, indicative of MT polymerization events (Figure 5A, middle and right panels). The MT signal increased by 0.06/min for 20 min and saturated at 2.3 ± 0.59 times of pre-aspiration levels after 30 min (Figure 5B). The aspirated cells displayed a 2.0 ± 0.38-fold asymmetry of fluorescence signal between the aspirated part and the non-affected basal part within 30 min (Figure 5A right panel, Figure 5C). To discard possible unspecific increases of GFP signal induced by the stretching, we used *UBQ10::Venus-TUA6*, which showed the same effect, and actin marker Fimbrin-YFP and *35S::GFP* (free cytosolic GFP), both showing no increase of fluorescence signal upon aspiration, respectively (Figures S5A–S5G). We used propidium iodide (PI) staining to investigate whether the aspirated cells remained viable during stretching. PI stains the cell walls of healthy cells and passes through the membranes of harmed or dead cells, where it strongly stains the cell interior. During the aspiration experiments, we did not observe any increased PI fluorescence
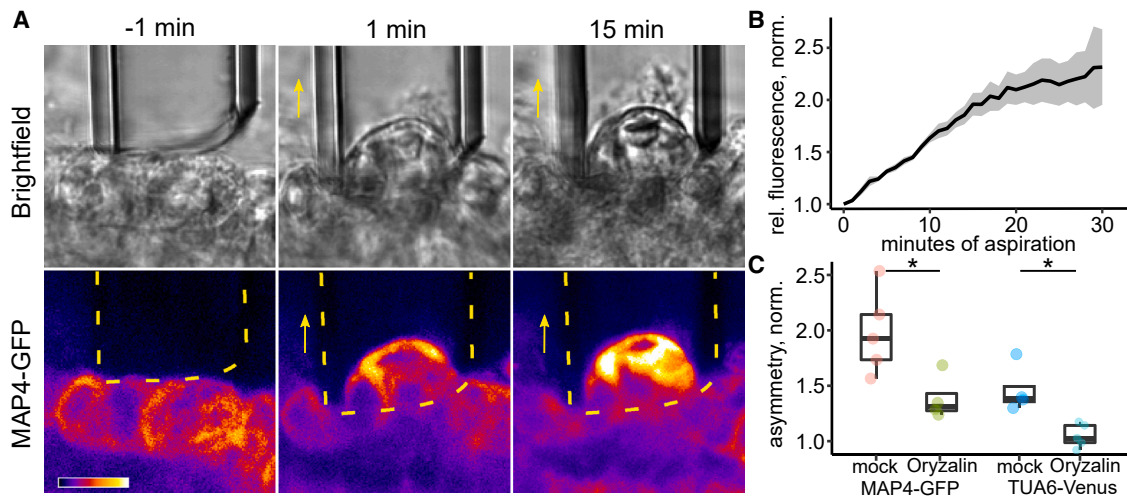
Figure 5. Induction of cell-localized MT polymerization by aspiration

(A) Aspiration of epidermal cells. Top row: brightfield; bottom row: 35S::MAP4-GFP fluorescence before (left), at the beginning (middle), and after 15 min (right) of aspiration. Yellow arrow marks the direction of aspiration and the yellow dotted line indicates the position of the pipette.

(B) Time series of 35S::MAP4-GFP signal in aspirated epidermal cells (n = 5 cells). Data are represented as mean from individual cells over time (mean gray value relative to t_0, normalized by direct neighboring cell) and lighter background indicates standard error.

(C) Quantification of 35S::MAP4-GFP (left) and UBQ10::Venus-TUA6 (right) fluorescence of aspirated parts relative to non-aspirated part (= asymmetry) of epidermal cells during mock and 5 μM oryzalin treatment (n = 4–5 cells each). Data are normalized to the closest non-aspirated neighbor.

See also Figure S5.

within the aspirated cells (Figure S5H). To test, whether the increased fluorescence came from an increase of MT polymerization, we treated plants with oryzalin as a depolymerization drug and performed aspiration on epidermal cells, resulting in no increase of fluorescence over time and no asymmetry between aspirated and non-aspirated parts (Figures 5C, S5A, S5C, and S5F). This indicates that the observed effect is specific to the formation of MT bundles and supports our previous findings that mechanical forces underlying stretching increase MT stability.

Thus, externally applied, micropipette aspiration-assisted cell stretching leads to immediate local MT stabilization, supporting a direct link between mechanical forces and MT polymerization.

Mechanical forces alter MT stability and drive division plane changes

Our experiments suggest that mechanical stress from stretching directly causes MT stabilization. This suggests that deformation and cell expansion after wounding predictably alter MT stability and orientation, subsequently driving division plane changes.

To visualize these effects, we quantified expansion and MT abundance changes over time from the same ablation site and represented them in a single, schematic image (Figure 6). The ablation of epidermal cells was followed by an immediate deformation of the adjacent cells due to the pressure drop from the collapsed cell. The pressure drop also changed mechanical forces within the root, leading to increased cell wall extension of up to 2-fold within 12 h in transversal walls perpendicular to the wound area. The stretched transversal membranes show the strongest increase of cortical MT abundance over time (up to 1.2-fold), while non-stretched membranes remained unaffected and lost MT fluorescence signal over time (up to 0.5-fold).

The increased abundance at stretched, transversal membranes led to the occurrence of multidirectional MT arrays, with longitudinal/transversal MT ratios of 1.17 up to 1.43 in fully stretched cells, whereas non-stretched cells displayed ratios of 0.87 and below. Cells with longitudinal/transversal ratios of above 1.0 changed division planes from anticlinal (transversal) to periclinal (longitudinal), whereas cells with ratios below 1.0 maintained the normally occurring, anticlinal (transversal) division planes. In a complementary quantification, we visualized the deformations of cells under aspiration and the consequent change of MT stability in aspirated cells. We found that the cell wall directly next to the tip of the pipette is stretched between 1.3- and 1.9-fold during the aspiration, and cytosolic MT intensity increases in the adjacent area between 1.7- and 1.9-fold (Figures S6A and S6B).

These results show the direct connection of mechanical forces, here manipulated by cell ablation, with MT stability and orientation impacting division plane selection.

DISCUSSION

In this work, we focus on one of the key questions of developmental biology, namely how plant cells can switch their division planes—a key process by which plant tissues and organs are shaped. We addressed this question in the context of restorative cell divisions during wound healing and tissue reconstruction in *Arabidopsis* root. We found that it is the direction of cellular growth and resulting mechanical forces that directly affect cortical MT stability/polymerization, leading to the reorientation of MT arrays and ultimately new cell division planes. These data provide key insights toward understanding how cell division orientation can be flexibly rearranged in response
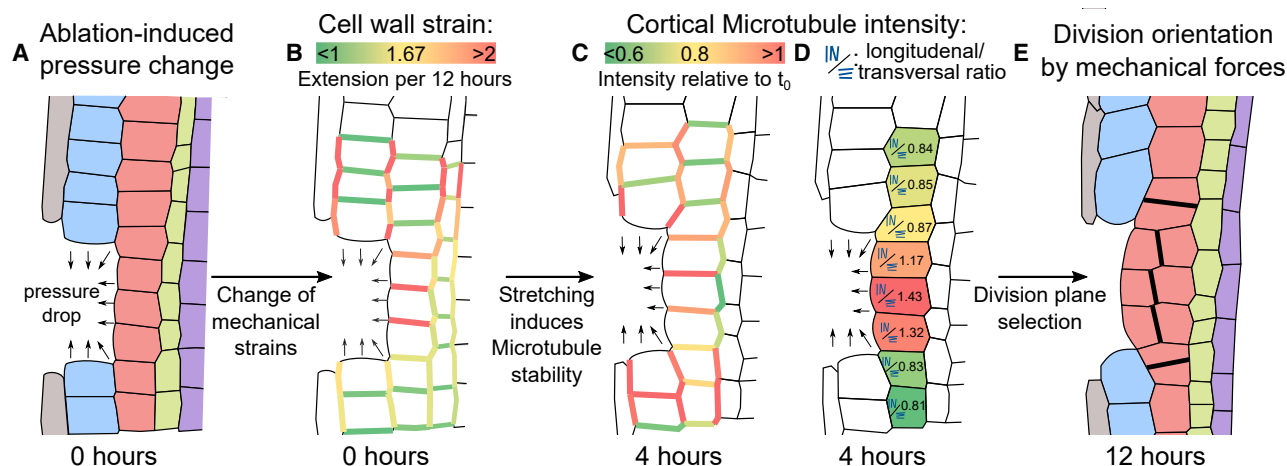
Figure 6. Schematic summary of mechanical effects after ablation on MT stability and orientation
Representative ablation of epidermal cells followed by expansion of cortical cells and changes in MT stability and orientation leading to changes in division plane orientation. From left to right: (A) Redrawn and colorized confocal image of an epidermal ablation 10 min after ablation. (B) Cell outlines and cell wall strain (as measured by relative cell wall extension after 12 h) 10 min after ablation. (C) Cell outlines and cortical MT intensity (measured as mean gray membrane signal relative to t_0) 4 h after ablation. (D) Cell outlines and longitudinal/transversal MT array ratio (as measured by mean gray value on apical and basal relative to transversal membranes). Small arrows indicate pressure changes. (E) Redrawn and colorized confocal image 12 h after ablation showing new division planes as thick black lines. Cells were re-colorized as epidermis (blue), cortex (red), endodermis (green), and pericycle (purple).
See also Figure S6.

to mechanical forces within a tissue and thus determine the plant architecture.

Cell wall transmits mechanical tension for re-arrangement of cell growth
Plant cells are encapsulated by the cell wall, a cellular component that glues neighboring cells together and prevents cell migration. Following wounding, adjacent cells, and their neighbors are deformed and stretched toward the wound area. This shows that the cell wall in roots is sufficiently plastic to transmit mechanical forces across the tissue and that deformation likely manifests because the root tissues underlying the epidermis are under compression—similar to what was shown for the hypocotyl.[47] Extended cells undergo division plane changes, implying the importance of wounding-induced deformations for tissue-restoration capacity. Notably, inner cell types deform more toward the wound than outer cells, suggesting a greater extendibility and compression of inner tissues. Differential stiffness of certain cell walls in the root has been predicted,[46] though experimental data has yet to support this idea.[57] Here, we observe a compression of inner root tissue leading to differential extendibility in the root cell wall matrix and show its relevance for developmental processes, like wound healing and division plane determination. In this process, the compression helps to ensure that wounds will be mainly healed from the inside and not the outside.

Direction of cell expansion strictly correlates with MT orientations and cell division orientation
The high turgor pressure of plant cells requires strong cell walls, which typically limit cellular expansion to occur in only one pre-defined direction. An ablation causes a pressure drop at the wound site, altering mechanical stress at the organ scale and allowing alternative directions of cell expansion toward the wound. The expansion of wound-adjacent cells is accompanied by a re-arrangement of cortical MT arrays in two different directions: perpendicular to the main growth axis of the root (as in the undisturbed situation) and perpendicular to the direction of altered cell expansion (toward the wound). Notably, these orientations persist after depolymerization and re-polymerization of MTs. This supports the idea that cells sense the change in the stress patterns present at the organ scale at any time during the growth process and align MT orientations accordingly.[31,40,58] Hence, division planes in the root meristem align perpendicular to the direction of maximum growth, as seen in undisturbed situations, and perpendicular to pressure changes through wounding or other more physiological events, altering division plane orientation by physical effects alone.

Cellular tensions rapidly drive MT polymerization
Wounding causes a local pressure drop that deforms the surrounding cells and leads to cell expansion in a new direction. The deformation causes rapid stretching of cell sides toward the wound. The immediate *de novo* MT polymerization and subsequent increase in abundance of cortical MT arrays at stretched sides suggests a direct link between mechanical forces of stretching with MT nucleation and stability. Alterations of MT orientation and bundling after mechanical perturbations have been hypothesized and demonstrated in recent years.[30,32,33] More specifically, *in vitro* studies have suggested a connection of mechanical forces to MT polymerization,[42–45] and recent *in vivo* studies on isolated protoplasts have shown that MTs dynamically change orientation upon alteration of geometry and tensile stress.[31,59] However, *in vivo* investigation of MT stability alterations in direct response to a change in mechanical stress has so far been lacking.

We developed an approach of plant-cell aspiration to show that induced cell wall strain is sufficient to stabilize MT polymerization, leading to the formation of MT bundles. The purely mechanical stimulation causes MT polymerization in stretched parts of the cell, whereas non-aspirated parts remain unaffected. Such a fast and dynamic response of the MT cytoskeleton upon mechanical manipulation has been reported also for leaf epidermal cells that were locally compressed by probing with a microneedle.[60] Similarly, after cell collapse, stretched cell sides show increased MT stability, while non-stretched sides remained unaffected. Over time, the constant stretching changes MT array distribution and eventually results in MT reorientation. Similar responses in MT arrangement were observed while applying tensile stress in hypocotyls,[61] or compression of hypocotyls[35] or the apical meristem.[33] Our data from internally and externally manipulated root cells provide evidence for a regulation of MT array formation by a directional cell stretching, thus constituting a mechanism of how cell growth via MT stabilization can rearrange MT orientation, which can then determine cell division orientation.

We identified a mechanism linking directional cell growth and orientation of cell division that depends exclusively on mechanical forces. These forces can be transmitted by the cell wall matrix, with differential extendibility that allows cell stretching, and is sensed through variations in MT stability/polymerization, leading to MT reorientation and, ultimately, determination of the cell division plane. We demonstrated and visualized an interdependence of mechanical forces and MT polymerization *in vivo*. The underlying molecular mechanism linking both processes may or may not require other cellular components, i.e., cell wall receptors or MT-associated proteins. Overall, these findings show how directional cell expansion, via MT stabilization and reorientation, rearranges cell division planes, which ultimately determines tissue and plant architecture.

Limitations of the study

The here-presented study shows how MT filaments are stabilized after high tension, informing plant-cell division planes. We investigated this phenomenon in the context of meristematic cells in the root tip. The small and packed cells in the root meristem represent a technical challenge for real-time imaging of organized MT bundles within individual cells. Hence, we used cell-boundary-associated fluorescence signals as an estimation of the accumulation of cortical bundles to overcome this challenge. The existence of very small cells close to the stem cell niche and already-elongating cells in the older meristematic area contributes to an interesting and complex, yet undescribed, biomechanical behavior of the root tip. We estimated the mechanical properties of the root cells by quantifying extendibility after big-area ablations; however, further studies may be required to deepen our understanding of the physical interactions present and how they influence cellular and organ growth in the root.

STAR★METHODS

Detailed methods are provided in the online version of this paper and include the following:

- KEY RESOURCES TABLE
- RESOURCE AVAILABILITY
  - Lead contact
  - Materials availability
  - Data and code availability
- EXPERIMENTAL MODEL AND STUDY PARTICIPANT DETAILS
  - Plant material
  - Growth conditions
- METHOD DETAILS
  - Pharmacological treatments
  - Sample preparation
  - Confocal imaging and image processing
  - MorphoGraphX image analysis
  - Spinning disk imaging
  - Vertical stage microscopy, root tracking and image processing
  - UV laser ablation setup
  - Aspiration setup
  - Wounded root extraction
- QUANTIFICATION AND STATISTICAL ANALYSIS
  - Spindle and phragmoplast angles
  - Periclinal divisions
  - Fluorescence intensity in single cells within time series
  - Cell expansion
  - MT intensity within time series
  - MT intensity ratios
  - MT intensity within aspiration assays

AUTHOR CONTRIBUTIONS

L.H., S.Y., P.M., and J.F. initiated the project. L.H., J.C.M., and J.F. designed experiments. L.H., L.S., and S.C.-M. performed experiments. L.H., N.T., and M.M. analyzed the data. L.H. and J.F. wrote the manuscript. J.C.M., N.T., and M.M. edited the manuscript. E.B. and C.-P.H., helped with supervising the project. L.H., M.M., Y.D., and J.F. acquired funding.

REFERENCES

1. van den Berg, C., Willemsen, V., Hage, W., Weisbeek, P., and Scheres, B. (1995). Cell fate in the Arabidopsis root meristem determined by directional signalling. Nature *378*, 62–65. https://doi.org/10.1038/378062a0.

2. Dolan, L., Janmaat, K., Willemsen, V., Linstead, P., Poethig, S., Roberts, K., and Scheres, B. (1993). Cellular organisation of the Arabidopsis thaliana root. Development *119*, 71–84. https://doi.org/10.1242/dev.119.1.71.

3. Rasmussen, C.G., and Bellinger, M. (2018). An overview of plant division-plane orientation. New Phytol. *219*, 505–512. https://doi.org/10.1111/nph.15183.

4. Hoermayer, L., and Friml, J. (2019). Targeted cell ablation-based insights into wound healing and restorative patterning at Elsevier Ltd. Curr Opin Plant Biol. *52*, 124–130. https://doi.org/10.1016/j.pbi.2019.08.006.

5. Ikeuchi, M., Favero, D.S., Sakamoto, Y., Iwase, A., Coleman, D., Rymen, B., and Sugimoto, K. (2019). Molecular Mechanisms of Plant Regeneration. Annu. Rev. Plant Biol. *70*, 377–406. https://doi.org/10.1146/annurev-arplant-050718-100434.

6. Bloch, R. (1941). Wound healing in higher plants. Bot. Rev. *7*, 110–146. https://doi.org/10.1007/BF02872446.

7. Marhava, P., Hoermayer, L., Yoshida, S., Marhavý, P., Benková, E., and Friml, J. (2019). Re-activation of Stem Cell Pathways for Pattern Restoration in Plant Wound Healing. Cell *177*, 957–969.e13. https://doi.org/10.1016/j.cell.2019.04.015.

8. Hoermayer, L., Montesinos, J.C., Marhava, P., Benková, E., Yoshida, S., and Friml, J. (2020). Wounding-induced changes in cellular pressure and localized auxin signalling spatially coordinate restorative divisions in roots. Proc. Natl. Acad. Sci. USA *117*, 15322–15331. https://doi.org/10.1073/PNAS.2003346117.

9. Efroni, I., Mello, A., Nawy, T., Ip, P.L., Rahni, R., Delrose, N., Powers, A., Satija, R., and Birnbaum, K.D. (2016). Root Regeneration Triggers an Embryo-like Sequence Guided by Hormonal Interactions. Cell *165*, 1721–1733. https://doi.org/10.1016/j.cell.2016.04.046.

10. Sena, G., Wang, X., Liu, H.-Y., Hofhuis, H., and Birnbaum, K.D. (2009). Organ regeneration does not require a functional stem cell niche in plants. Nature *457*, 1150–1153. https://doi.org/10.1038/nature07597.

11. Xu, J., Hofhuis, H., Heidstra, R., Sauer, M., Friml, J., and Scheres, B. (2006). A molecular framework for plant regeneration. Science *311*, 385–388. https://doi.org/10.1126/science.1121790.

12. De Rybel, B., Möller, B., Yoshida, S., Grabowicz, I., Barbier de Reuille, P., Boeren, S., Smith, R.S., Borst, J.W., and Weijers, D. (2013). A bHLH Complex Controls Embryonic Vascular Tissue Establishment and Indeterminate Growth in Arabidopsis. Dev. Cell *24*, 426–437. https://doi.org/10.1016/J.DEVCEL.2012.12.013.

13. De Rybel, B., Mähönen, A.P., Helariutta, Y., and Weijers, D. (2016). Plant vascular development: from early specification to differentiation. Nat. Rev. Mol. Cell Biol. *17*, 30–40. https://doi.org/10.1038/nrm.2015.6.

14. Vilches Barro, A., Stöckle, D., Thellmann, M., Ruiz-Duarte, P., Bald, L., Louveaux, M., von Born, P., Denninger, P., Goh, T., Fukaki, H., et al. (2019). Cytoskeleton Dynamics Are Necessary for Early Events of Lateral Root Initiation in Arabidopsis. Curr. Biol. *29*, 2443–2454.e5. https://doi.org/10.1016/J.CUB.2019.06.039.

15. Dubrovsky, J.G., Sauer, M., Napsucialy-Mendivil, S., Ivanchenko, M.G., Friml, J., Shishkova, S., Celenza, J., and Benková, E. (2008). Auxin acts as a local morphogenetic trigger to specify lateral root founder cells. Proc. Natl. Acad. Sci. USA *105*, 8790–8794. https://doi.org/10.1073/PNAS.0712307105.

16. Marhavý, P., Montesinos, J.C., Abuzeineh, A., Van Damme, D., Vermeer, J.E.M., Duclercq, J., Rakusová, H., Nováková, P., Friml, J., Geldner, N., and Benková, E. (2016). Targeted cell elimination reveals an auxin-guided biphasic mode of lateral root initiation. Genes Dev. *30*, 471–483. https://doi.org/10.1101/gad.276964.115.

17. Besson, S., and Dumais, J. (2011). Universal rule for the symmetric division of plant cells. Proc. Natl. Acad. Sci. USA *108*, 6294–6299. https://doi.org/10.1073/pnas.1011866108.

18. Errera, L. (1888). Uber zellformen und seifenblasen. Bot. Zentralbl. *34*, 395–398.

19. van Damme, D., de Rybel, B., Gudesblat, G., Demidov, D., Grunewald, W., de Smet, I., Houben, A., Beeckman, T., and Russinova, E. (2011). Arabidopsis α Aurora kinases function in formative cell division plane orientation. Plant Cell *23*, 4013–4024. https://doi.org/10.1105/TPC.111.089565.

20. Yoshida, S., Barbier de Reuille, P., Lane, B., Bassel, G.W., Prusinkiewicz, P., Smith, R.S., and Weijers, D. (2014). Genetic Control of Plant Development by Overriding a Geometric Division Rule. Dev. Cell *29*, 75–87. https://doi.org/10.1016/J.DEVCEL.2014.02.002.

21. Heidstra, R., Welch, D., and Scheres, B. (2004). Mosaic analyses using marked activation and deletion clones dissect Arabidopsis SCARECROW action in asymmetric cell division. Genes Dev. *18*, 1964–1969. https://doi.org/10.1101/GAD.305504.

22. Helariutta, Y., Fukaki, H., Wysocka-Diller, J., Nakajima, K., Jung, J., Sena, G., Hauser, M.T., and Benfey, P.N. (2000). The SHORT-ROOT Gene Controls Radial Patterning of the Arabidopsis Root through Radial Signaling. Cell *101*, 555–567. https://doi.org/10.1016/S0092-8674(00)80865-X.

23. Willemsen, V., Bauch, M., Bennett, T., Campilho, A., Wolkenfelt, H., Xu, J., Haseloff, J., and Scheres, B. (2008). The NAC Domain Transcription Factors FEZ and SOMBRERO Control the Orientation of Cell Division Plane in Arabidopsis Root Stem Cells. Dev. Cell *15*, 913–922. https://doi.org/10.1016/J.DEVCEL.2008.09.019.

24. Rodriguez-Furlan, C., Campos, R., Toth, J.N., and Van Norman, J.M. (2022). Distinct mechanisms orchestrate the contra-polarity of IRK and KOIN, two LRR-receptor-kinases controlling root cell division. Nat. Commun. *13*, 235. https://doi.org/10.1038/s41467-021-27913-1.

25. Canher, B., Heyman, J., Savina, M., Devendran, A., Eekhout, T., Vercauteren, I., Prinsen, E., Matosevich, R., Xu, J., Mironova, V., and De Veylder, L. (2020). Rocks in the auxin stream: Wound-induced auxin accumulation and ERF115 expression synergistically drive stem cell regeneration. Proc. Natl. Acad. Sci. USA *117*, 16667–16677. https://doi.org/10.1073/PNAS.2006620117.

26. Heyman, J., Cools, T., Canher, B., Shavialenka, S., Traas, J., Vercauteren, I., Van den Daele, H., Persiau, G., De Jaeger, G., Sugimoto, K., and De Veylder, L. (2016). The heterodimeric transcription factor complex ERF115–PAT1 grants regeneration competence. Nat. Plants *2*, 16165. https://doi.org/10.1038/nplants.2016.165.

27. McQueen-Mason, S., Durachko, D.M., and Cosgrove, D.J. (1992). Two endogenous proteins that induce cell wall extension in plants. Plant Cell *4*, 1425–1433. https://doi.org/10.1105/TPC.4.11.1425.

28. Zerzour, R., Kroeger, J., and Geitmann, A. (2009). Polar growth in pollen tubes is associated with spatially confined dynamic changes in cell mechanical properties. Dev. Biol. *334*, 437–446. https://doi.org/10.1016/J.YDBIO.2009.07.044.

29. Saab, I.N., Sharp, R.E., Pritchard, J., and Voetberg, G.S. (1990). Increased endogenous abscisic Acid maintains primary root growth and inhibits shoot growth of maize seedlings at low water potentials. Plant Physiol. *93*, 1329–1336. https://doi.org/10.1104/PP.93.4.1329.

30. Sampathkumar, A., Krupinski, P., Wightman, R., Milani, P., Berquand, A., Boudaoud, A., Hamant, O., Jönsson, H., and Meyerowitz, E.M. (2014). Subcellular and supracellular mechanical stress prescribes cytoskeleton behavior in Arabidopsis cotyledon pavement cells. eLife *3*, e01967. https://doi.org/10.7554/eLife.01967.

31. Colin, L., Chevallier, A., Tsugawa, S., Gacon, F., Godin, C., Viasnoff, V., Saunders, T.E., and Hamant, O. (2020). Cortical tension overrides geometrical cues to orient microtubules in confined protoplasts. Proc. Natl. Acad. Sci. USA *117*, 32731–32738. https://doi.org/10.1073/pnas.2008895117.

32. Louveaux, M., Julien, J.-D., Mirabet, V., Boudaoud, A., and Hamant, O. (2016). Cell division plane orientation based on tensile stress in

Arabidopsis thaliana. Proc. Natl. Acad. Sci. USA *113*, E4294–E4303. https://doi.org/10.1073/PNAS.1600677113.

33. Hamant, O., Heisler, M.G., Jönsson, H., Krupinski, P., Uyttewaal, M., Bokov, P., Corson, F., Sahlin, P., Boudaoud, A., Meyerowitz, E.M., et al. (2008). Developmental patterning by mechanical signals in Arabidopsis. Science *322*, 1650–1655. https://doi.org/10.1126/science.1165594.

34. Verger, S., Long, Y., Boudaoud, A., and Hamant, O. (2018). A tension-adhesion feedback loop in plant epidermis. eLife *7*, e34460. https://doi.org/10.7554/eLife.34460.

35. Robinson, S., and Kuhlemeier, C. (2018). Global Compression Reorients Cortical Microtubules in Arabidopsis Hypocotyl Epidermis and Promotes Growth. Curr. Biol. *28*, 1794–1802.e2. https://doi.org/10.1016/J.CUB.2018.04.028.

36. Hervieux, N., DuMond, M., Sapala, A., Routier-Kierzkowska, A.L., Kierzkowski, D., Roeder, A.H.K., Smith, R.S., Boudaoud, A., and Hamant, O. (2016). A Mechanical Feedback Restricts Sepal Growth and Shape in Arabidopsis. Curr. Biol. *26*, 1019–1028. https://doi.org/10.1016/J.CUB.2016.03.004.

37. Hervieux, N., Tsugawa, S., Fruleux, A., DuMond, M., Routier-Kierzkowska, A.L., Komatsuzaki, T., Boudaoud, A., Larkin, J.C., Smith, R.S., Li, C.B., and Hamant, O. (2017). Mechanical Shielding of Rapidly Growing Cells Buffers Growth Heterogeneity and Contributes to Organ Shape Reproducibility. Curr. Biol. *27*, 3468–3479.e4. https://doi.org/10.1016/J.CUB.2017.10.033.

38. Jacques, E., Verbelen, J.P., and Vissenberg, K. (2013). Mechanical stress in Arabidopsis leaves orients microtubules in a "continuous" supracellular pattern. BMC Plant Biol. *13*, 163. https://doi.org/10.1186/1471-2229-13-163.

39. Trinh, D.-C., Alonso-Serra, J., Asaoka, M., Colin, L., Cortes, M., Malivert, A., Takatani, S., Zhao, F., Traas, J., Trehin, C., and Hamant, O. (2021). How Mechanical Forces Shape Plant Organs. Curr Biol. *31*, R143–R159. https://doi.org/10.1016/j.cub.2020.12.001.

40. Kropf, D.L., Bisgrove, S.R., and Hable, W.E. (1998). Cytoskeletal control of polar growth in plant cells. Curr. Opin. Cell Biol. *10*, 117–122. https://doi.org/10.1016/S0955-0674(98)80094-X.

41. Rasmussen, C.G., Humphries, J.A., and Smith, L.G. (2011). Determination of symmetric and asymmetric division planes in plant cells. Annu. Rev. Plant Biol. *62*, 387–409. https://doi.org/10.1146/annurev-arplant-042110-103802.

42. Kabir, A.M.R., Inoue, D., Hamano, Y., Mayama, H., Sada, K., and Kakugo, A. (2014). Biomolecular Motor Modulates Mechanical Property of Microtubule. Biomacromolecules *15*, 1797–1805. https://doi.org/10.1021/BM5001789.

43. Franck, A.D., Powers, A.F., Gestaut, D.R., Gonen, T., Davis, T.N., and Asbury, C.L. (2007). Tension applied through the Dam1 complex promotes microtubule elongation providing a direct mechanism for length control in mitosis. Nat. Cell Biol. *9*, 832–837. https://doi.org/10.1038/ncb1609.

44. Trushko, A., Schäffer, E., and Howard, J. (2013). The growth speed of microtubules with XMAP215-coated beads coupled to their ends is increased by tensile force. Proc. Natl. Acad. Sci. USA *110*, 14670–14675. https://doi.org/10.1073/PNAS.1218053110.

45. Hamant, O., Inoue, D., Bouchez, D., Dumais, J., and Mjolsness, E. (2019). Are microtubules tension sensors? Nat. Commun. *10*, 2360. https://doi.org/10.1038/s41467-019-10207-y.

46. Fridman, Y., Strauss, S., Horev, G., Ackerman-Lavert, M., Reiner-Benaim, A., Lane, B., Smith, R.S., and Savaldi-Goldstein, S. (2021). The root meristem is shaped by brassinosteroid control of cell geometry. Nat. Plants *7*, 1475–1484. https://doi.org/10.1038/s41477-021-01014-9.

47. Kutschera, U., and Niklas, K.J. (2007). The epidermal-growth-control theory of stem elongation: an old and a new perspective. J. Plant Physiol. *164*, 1395–1409. https://doi.org/10.1016/J.JPLPH.2007.08.002.

48. Asaoka, M., Sakamoto, S., Gunji, S., Mitsuda, N., Tsukaya, H., Sawa, S., Hamant, O., and Ferjani, A. (2023). Contribution of vasculature to stem integrity in Arabidopsis thaliana. Development *150*, dev201156. https://doi.org/10.1242/DEV.201156.

49. Marc, J., Granger, C.L., Brincat, J., Fisher, D.D., Kao, Th., McCubbin, A.G., and Cyr, R.J. (1998). A GFP-MAP4 reporter gene for visualizing cortical microtubule rearrangements in living epidermal cells. Plant Cell *10*, 1927–1940. https://doi.org/10.1105/tpc.10.11.1927.

50. Ubeda-Tomás, S., Federici, F., Casimiro, I., Beemster, G.T.S., Bhalerao, R., Swarup, R., Doerner, P., Haseloff, J., and Bennett, M.J. (2009). Gibberellin Signaling in the Endodermis Controls Arabidopsis Root Meristem Size. Curr. Biol. *19*, 1194–1199. https://doi.org/10.1016/J.CUB.2009.06.023.

51. Schaefer, E., Belcram, K., Uyttewaal, M., Duroc, Y., Goussot, M., Legland, D., Laruelle, E., de Tauzia-Moreau, M.-L., Pastuglia, M., and Bouchez, D. (2017). The preprophase band of microtubules controls the robustness of division orientation in plants. Science *356*, 186–189. https://doi.org/10.1126/SCIENCE.AAL3016.

52. Morejohn, L.C., and Fosket, D.E. (1991). The biochemistry of compounds with anti-microtubule activity in plant cells. Pharmacol. Ther. *51*, 217–230. https://doi.org/10.1016/0163-7258(91)90078-Z.

53. Fendrych, M., Akhmanova, M., Merrin, J., Glanc, M., Hagihara, S., Takahashi, K., Uchida, N., Torii, K.U., and Friml, J. (2018). Rapid and reversible root growth inhibition by TIR1 auxin signaling. Nat. Plants *4*, 453–459. https://doi.org/10.1038/s41477-018-0190-1.

54. Montesinos, J.C., Abuzeineh, A., Kopf, A., Juanes-Garcia, A., Ötvös, K., Petrášek, J., Sixt, M., and Benková, E. (2020). Phytohormone cytokinin guides microtubule dynamics during cell progression from proliferative to differentiated stage. EMBO J. *39*, e104238. https://doi.org/10.15252/embj.2019104238.

55. Scheible, W.-R., Eshed, R., Richmond, T., Delmer, D., and Somerville, C. (2001). Modifications of cellulose synthase confer resistance to isoxaben and thiazolidinone herbicides in Arabidopsis Ixr1 mutants. Proc. Natl. Acad. Sci. USA *98*, 10079–10084. https://doi.org/10.1073/PNAS.191361598.

56. Maître, J.L., Berthoumieux, H., Krens, S.F.G., Salbreux, G., Jülicher, F., Paluch, E., and Heisenberg, C.P. (2012). Adhesion functions in cell sorting by mechanically coupling the cortices of adhering cells. Science *338*, 253–256. https://doi.org/10.1126/science.1225399.

57. Elsayad, K., Werner, S., Gallemí, M., Kong, J., Sánchez Guajardo, E.R.S., Zhang, L., Jaillais, Y., Greb, T., and Belkhadir, Y. (2016). Mapping the subcellular mechanical properties of live cells in tissues with fluorescence emission-Brillouin imaging. Sci. Signal. *9*, rs5. https://doi.org/10.1126/scisignal.aaf6326.

58. Moulia, B., Douady, S., and Hamant, O. (2021). Fluctuations shape plants through proprioception. Science *372*, eabc6868. https://doi.org/10.1126/SCIENCE.ABC6868.

59. Durand-Smet, P., Spelman, T.A., Meyerowitz, E.M., and Jönsson, H. (2020). Cytoskeletal organization in isolated plant cells under geometry control. Proc. Natl. Acad. Sci. USA *117*, 17399–17408. https://doi.org/10.1073/PNAS.2003184117.

60. Hardham, A.R., Takemoto, D., and White, R.G. (2008). Rapid and dynamic subcellular reorganization following mechanical stimulation of Arabidopsis epidermal cells mimics responses to fungal and oomycete attack. BMC Plant Biol. *8*, 63. https://doi.org/10.1186/1471-2229-8-63.

61. Hejnowicz, Z., Rusin, A., and Rusin, T. (2000). Tensile tissue stress affects the orientation of cortical microtubules in the epidermis of sunflower hypocotyl. J. Plant Growth Regul. *19*, 31–44. https://doi.org/10.1007/s003440000005.

62. Camilleri, C., Azimzadeh, J., Pastuglia, M., Bellini, C., Grandjean, O., and Bouchez, D. (2002). The Arabidopsis TONNEAU2 Gene Encodes a Putative Novel Protein Phosphatase 2A Regulatory Subunit Essential for the Control of the Cortical Cytoskeleton. Plant Cell *14*, 833–845. https://doi.org/10.1105/TPC.010402.

63. Toyota, M., Spencer, D., Sawai-Toyota, S., Jiaqi, W., Zhang, T., Koo, A.J., Howe, G.A., and Gilroy, S. (2018). Glutamate triggers long-distance, calcium-based plant defense signaling. Science *361*, 1112–1115. https://doi.org/10.1126/science.aat7744.

64. Wang, Y.S., Motes, C.M., Mohamalawari, D.R., and Blancaflor, E.B. (2004). Green fluorescent protein fusions to Arabidopsis Fimbrin 1 for spatio-temporal imaging of F-actin dynamics in roots. Cell Motil. Cytoskeleton *59*, 79–93. https://doi.org/10.1002/CM.20024.

65. Geldner, N., Dénervaud-Tendon, V., Hyman, D.L., Mayer, U., Stierhof, Y.D., and Chory, J. (2009). Rapid, combinatorial analysis of membrane compartments in intact plants with a multicolor marker set. Plant J. *59*, 169–178. https://doi.org/10.1111/j.1365-313X.2009.03851.x.

66. Salanenka, Y., Verstraeten, I., Löfke, C., Tabata, K., Naramoto, S., Glanc, M., and Friml, J. (2018). Gibberellin DELLA signaling targets the retromer complex to redirect protein trafficking to the plasma membrane. Proc. Natl. Acad. Sci. USA *115*, 3716–3721. https://doi.org/10.1073/pnas.1721760115.

67. Jakobs, M.A.H., Dimitracopoulos, A., and Franze, K. (2019). Kymobutler, a deep learning software for automated kymograph analysis. eLife *8*, e42288. https://doi.org/10.7554/eLife.42288.

68. Thévenaz, P., Ruttimann, U.E., and Unser, M. (1998). A pyramid approach to subpixel registration based on intensity. IEEE Trans. Image Process. *7*, 27–41. https://doi.org/10.1109/83.650848.

69. Marhavý, P., and Benková, E. (2015). Real-time Analysis of Lateral Root Organogenesis in Arabidopsis. Bio Protoc. *5*, 5. https://doi.org/10.21769/bioprotoc.1446.

70. Strauss, S., Runions, A., Lane, B., Eschweiler, D., Bajpai, N., Trozzi, N., Routier-Kierzkowska, A.L., Yoshida, S., Rodrigues da Silveira, S.R., Vijayan, A., et al. (2022). Using positional information to provide context for biological image analysis with MorphoGraphX 2.0. eLife *11*, e72601. https://doi.org/10.7554/eLife.72601.

71. Glanc, M., Fendrych, M., and Friml, J. (2018). Mechanistic framework for cell-intrinsic re-establishment of PIN2 polarity after cell division at Palgrave. Nat Plants. *4*, 1082–1088. https://doi.org/10.1038/s41477-018-0318-3.

72. von Wangenheim, D., Hauschild, R., Fendrych, M., Barone, V., Benková, E., and Friml, J. (2017). Live tracking of moving samples in confocal microscopy for vertically grown roots. eLife *6*, e26792. https://doi.org/10.7554/eLife.26792.

73. Colombelli, J., Grill, S.W., and Stelzer, E.H.K. (2004). Ultraviolet diffraction limited nanosurgery of live biological tissues. Rev. Sci. Instrum. *75*, 472–478. https://doi.org/10.1063/1.1641163.

STAR★METHODS

KEY RESOURCES TABLE

REAGENT or RESOURCE	SOURCE	IDENTIFIER
Chemicals, peptides, and recombinant proteins		
Propidium iodide	Thermo Scientific	Cat#P3566
1-Naphthylacetic acid	Sigma-Aldrich	Cat#N0640
Isoxaben	Sigma-Aldrich	Cat#36138
Latrunculin B	Sigma-Aldrich	Cat#L5288
Oryzalin	Sigma-Aldrich	Cat#36182
Macerozyme R-10	Serva	Cat#28302
Experimental models: Organisms/strains		
Arabidopsis: WT Col-0	https://www.ncbi.nlm.nih.gov/Taxonomy/Browser/wwwtax.cgi	NCBI:txid3702
Arabidopsis: 35S::MAP4-GFP	Marc et al.,[49] Camilleri et al.[62]	Transgenic WS-4
Arabidopsis: CycB1;1::GFP	Ubeda-Tomás et al.[50]	Transgenic Col-0
Arabidopsis: 35S::GCaMP3	Toyota et al.[63]	Transgenic Col-0
Arabidopsis: 35S::Fimbrin-GFP	Wang et al.[64]	Transgenic Col-0
Arabidopsis: pUBQ10::EYFP-NPSN12 (W131Y)	Geldner et al.[65]	Transgenic Col-0
Arabidopsis: ERF115::NLS-GFP-GUS	Heyman et al.[26]	Transgenic Col-0
Arabidopsis: UBQ10::Venus-TUA6	Salanenka et al.[66]	Transgenic Col-0
Software and algorithms		
imageJ	https://imagej.net/Welcom/	RRID:SCR_003070
Zeiss Zen Software	https://www.zeiss.com/	N/A
R project	http://www.r-project.org/	RRID:SCR_001905
R-studio	https://www.rstudio.com/	RRID:SCR_000432
MorphoGraphX 2.0	https://morphographx.org/software/	N/A
Leica Application Suite X	https://www.leica-microsystems.com/	RRID:SCR_016555
Kymobutler	Jakobs et al.[67]	RRID:SCR_021717
TipTracker	https://elifesciences.org/articles/26792/figures#SD2-data	N/A
StackReg	Thevenaz et al.[68]	N/A
MultiStackReg	Thevenaz et al.[68]	RRID:SCR_016098
Imaris	https://imaris.oxinst.com/	RRID:SCR_007370

RESOURCE AVAILABILITY

Lead contact
Further information and requests for resources and reagents should be directed to and will be fulfilled by the lead contact, Jiří Friml(jiri.friml@ist.ac.at).

Materials availability
This study did not generate new unique reagents.

Data and code availability
- All data reported in this paper will be shared by the lead contact upon request.
- This paper does not report original code.
- Any additional information required to reanalyze the data reported in this paper is available from the lead contact upon request.

EXPERIMENTAL MODEL AND STUDY PARTICIPANT DETAILS

Plant material

Arabidopsis thaliana (L.) Heynh (accession Columbia-0) was used in this work (named WT). The following transgenic *Arabidopsis thaliana* lines were described previously:

35S::MAP4-GFP,[49,62] *CYCB1;1::GFP*,[50] "GCAMP" *35S::GCaMP3*,[63] *35S::Fimbrin-GFP*,[64] *W131Y*,[65] *ERF115::NLS-GFP-GUS*,[26] *UBQ10::Venus-TUA6*[66]

Growth conditions

Seeds of *A. thaliana* were surface sterilized with 70% ethanol, sown on Murashige and Skoog (1/2MS) medium (Duchefa) with 1% sucrose and 1% agar, stratified for 1-2 d and grown for 3-5 d at 21°C in a 16 hours light/8 hours dark cycle.

METHOD DETAILS

Pharmacological treatments

Seedlings were transferred on solid MS medium containing the indicated chemicals: propidium iodide (PI, 10 μM, Sigma-Aldrich or Thermofisher), Naphthylacetic acid (NAA, Duchefa Biochemie, final concentration 1 μM), Mannitol (Sigma-Aldrich, final concentration 0.2 M), Isoxaben (Sigma Aldrich, final concentration 10 μM), Latrunculin B (LatB, Sigma-Aldrich, final concentration 2 μM), Oryzalin (Duchefa Biochemie, final concentration 5 μM), Macerozyme R-10 (Serva, final concentration 1% w/v).

Sample preparation

Seedlings were placed on chambered cover glass (VWR, Kammerdeckgläser, Lab-Tek™, Nunc™ - eine kammer, catalog number: 734-2056) as described.[69] With the chamber, a block of solid MS media was cut out and PI solution was added. After the liquid soaked in, 10-15 seedlings were transferred to the agar and the block was inserted into the chamber. For FM4-64 staining, seedlings were incubated in FM4-64 staining solution (3 μg/ml in water) for 3 min and then placed on solid MS medium.

Confocal imaging and image processing

Confocal imaging was performed with Zeiss LSM700/800 inverted microscopes using 20x or 40x objectives. Detection of fluorescence signals was carried out for GFP (excitation 488 nm, emission 507 nm), YFP (excitation 514 nm, emission 527 nm) and PI or FM4-64 (excitation 536 nm, emission 617 nm). For fixed time point measurements, samples were observed 12 hours after ablation or at indicated time points. Images were analysed using the ImageJ (NIH; http://rsb.info.nih.gov/ij) and Zeiss Zen 2.3 "Black" or "Blue" software. Where necessary, images were processed by adjusting contrast and lightness and stacks were processed by sum slice operation to summarize multiple confocal planes or time points into one image. For 3D images, confocal (z) planes were chosen to fit ½ airy unit. To obtain top view images, z-stacks were processed using the "Reslice" tool. 3D images were analysed using Imaris software.

MorphoGraphX image analysis

Confocal signal was projected onto a mesh, and cells were segmented through seeding and Watershed Segmentation in MorphoGraphX 2.0. Post-wounding frames were parent-labeled to the timepoint prior wounding, and a heatmap was generated to visualize cell deformations. By identifying cell centroids and extracting their coordinates, Euclidean distances were computed to determine cell displacement.[70]

Spinning disk imaging

For the observation of immediate effects during/after ablation, an Andor spinning disk microscopy (CSU X-1, camera iXon 897 [back-thinned EMCCD], FRAPPA unit and motorized piezo stage) 63× water immersion objective was used. Videos were acquired with 1 focal plane, every 0.2 or 1.0 s. All images in a single experiment were captured with the same settings.

Vertical stage microscopy, root tracking and image processing

Vertical stage microscopy for long-term tracking of root meristems was performed as described.[7,71,72] Roots were imaged with a vertically positioned LSM700 or LSM800 inverted confocal microscope and Zeiss Zen 2.3 "Black" or "Blue" software, respectively, with 20x objective and detection of PI, GFP (see above) and transmitted light. Z-stacks of 30-42 μm were set accordingly to image each cell at least once. For the root-tracking, the TipTracker MATLAB script (Zen Black) or the TipTracker internal macro (Zen Blue) were used; interval duration was set between 600 s (10 min) and 720 s (12 min). The resulting images were concatenated and analysed using ImageJ. For registration, ImageJ macros "correct 3D drift", "StackReg[68]" or "MultiStackReg[68]" were used. Kymographs were generated using the "Reslice" tool.

UV laser ablation setup

The UV laser ablation was performed as described[7,16] which are based on a previously published layout.[73] The laser was applied in the upper corner of the cell of interest.

Aspiration setup

The aspiration setup was designed as previously described.[56] 10 or 20 μm glass pipettes (BioMedical Instruments) with 30° bent angle were filled with distilled water and then connected to a Microfluidic Flow Control System (Fluigent, Fluiwell), with negative pressure ranging from 7-750 Pa. The microfluidic setup was mounted on a micromanipulator (Eppendorf, Transferman NK2) and micropipette movement and pressure were controlled via a custom-programmed Labview (National Instruments) interface.

5-d old seedlings were transferred onto 1% Macerozyme and 0.2 M Mannitol containing agar medium. After 20 min the seedlings were transferred carefully to a 0.2 M Mannitol containing agar medium to recover from the cell wall digestion. Finally, the seedlings were transferred to liquid medium containing 0.2 M Mannitol in a MatTek 50mm Glass Bottom Dish, so that the cotyledons touched the glass and the root was facing towards the centre of the coverslip.

For the aspiration, the micropipette was placed touching a single epidermis cell in the centre of the root meristem and during imaging, full negative pressure (-750 Pa) was applied.

Imaging was performed using a Leica SP5 or a Leica Stellaris 5 confocal microscope with a resonant scanner and a Leica 20X, 0.7 NA objective, (Argon laser: 488 nm) for simultaneous imaging of fluorescent and brightfield channels.

Wounded root extraction

Seeds were sown on a sieve placed in a jar filled with MS medium to cover the seeds. After 4 weeks the root tips were harmed with a scalpel, and after 10 min incubation, the shoot was cut off and the roots were ground with a mortar and constantly cooled with liquid nitrogen. The root extract was stored at -80 °C. 5 ml of a phosphate buffer containing 38 mM KH_2PO_4 and 62 mM K_2HPO_4 were cooled to 4 °C and added to 1 g of the root extract. After an incubation time of 5 min, the suspension was centrifuged at 15000 g for 20 min at 4 °C. The supernatant was applied to growing 5-day-old seedlings (1 ml per hour to each root continuously for 12 hours).

QUANTIFICATION AND STATISTICAL ANALYSIS

Asterisks illustrate the p-value: $p < 0.001$ is ***, $p < 0.01$ is ** and $p < 0.05$ is *.

If not stated otherwise, statistical significance was computed using a Wilcoxon test.

Boxplots represent median +/- 95% confidence interval (=1.58*IQR/sqrt(n)).

If not stated otherwise (e.g., "representative example/replicate"), data shown was pooled from 3 technical replicates. Usually, 7-15 seedlings were used per experiment and condition, 1-2 ablation sites per root, depending on experiment 10-50% of ablation sites were quantifiable.

Spindle and phragmoplast angles

Spindle/phragmoplast angle was determined using the ImageJ "Angle" tool, taking the anticlinal walls as reference (0°). Data was plotted as histogram on a polar coordination system using R.

Periclinal divisions

Division events were counted by marking the time point at which a new cell wall (stained by PI) appeared in the first, inner adjacent cell of the ablation site. Only periclinal divisions (vertical cell walls) were counted. The percentage of cumulative division events over time was plotted using R.

Fluorescence intensity in single cells within time series

Signal intensity (mean grey value) from multi-stack (3D) videos in the green channel was quantified using ImageJ and recorded for each available time frame. To obtain relative values, the raw data was divided by the first time point value. Similarly, data from controls or reference cells (neighbouring and/or more distant cells) was recorded and the ratio of sample to reference value was calculated to obtain normalized values.

Cell expansion

Cell expansion within time series was approximated by the cell width, quantified as the distance between the midpoint of the inner and outer cell wall using ImageJ. Expansion values are relative to first time point and if indicated, normalized to neighbouring (reference) cells.

During fixed time points, cell expansion or initial displacement was approximated as the horizontal distance between the wound-adjacent membrane and the first, non-adjacent membrane of a neighbouring cell.

Expansion rates were determined from kymographs of growing root tips. One patch of cortex cells was registered over time, turned into a kymograph, coordinates of each line were obtained using Kymobutler,[67] and the rate of expansion was calculated from the slope of the lines.

MT intensity within time series

MT array intensity of a single cell was measured in a rectangular section from one confocal plane over time. All time frames were evaluated with the same selection.

MT bundle intensity of a single cell during collapse of the adjacent cell was measured in both, the first available time frame before collapse and after collapse and relative values were obtained by division. Values were normalized by division with values from neighbouring cells, not adjacent to collapsed cells.

MT intensity ratios

For lateral/apical membrane intensity ratio, MT intensity (*35S::MAP4-GFP, UBQ10::Venus-TUA6*) was measured on the apical membrane and on the lateral membrane not touching the wound. Reference/control cells were chosen from the same cell type of the same root further away from the wound (no visual deformations).

For lateral-membrane/cytosol intensity ratio, MT intensity (*35S::MAP4-GFP*, *UBQ10::Venus-TUA6*) was measured on the inner lateral membrane and in the cytosol excluding nucleus area.

MT intensity within aspiration assays

MT intensity (*35S::MAP4-GFP, UBQ10::Venus-TUA6*) in epidermis cells was measured in selections from one confocal plane over time. All time frames were evaluated with the same selection including reference cells (neighbouring, non-aspirated cells). Relative values were obtained from dividing by first value and normalized values from dividing by value from reference cells.